

The potential-energy tensors for subsystems. IV.

Homeoidally striated density profiles with a central cusp.

R. Caimmi and C. Marmo

Dipartimento di Astronomia, Università di Padova,
Vicolo Osservatorio 2, I-35122 Padova, Italy
caimmi@pd.astro.it – marmo@pd.astro.it

Received: Accepted:

Abstract. A general theory of homeoidally striated density profiles where no divergence occurs, is adapted to cuspy density profiles, with a suitable choice of the scaling density and the scaling radius. A general formulation of some physical parameters, such as angular-momentum vector, rotational-energy tensor (both calculated in connection with a special class of rotational velocity fields), inertia tensor, and self potential-energy tensor, is performed. Other potential-energy tensors involving two density profiles where the boundaries are similar and similarly placed, are also expressed. Explicit results are attained for three special cases of physical interest: NFW (e.g., Navarro et al. 1997) and MOA (e.g., Moore et al. 1999) density profiles, which fit to a good extent the results of high-resolution simulations for dark matter haloes, and H (Hernquist 1990) density profiles, which closely approximate the de Vaucouleurs $r^{1/4}$ law for elliptical galaxies. The virial theorem in tensor form for two-component systems is written for each subsystem, and applied to giant elliptical galaxies. The predicted velocity dispersion along the line of sight, in the limiting case where a principal axis points towards the observer, is found to be consistent with observations except for (intrinsic) $E7$ configurations where the major axis points towards the observer. If dark matter haloes host an amount of undetected baryons about twice as massive as the stellar subsystem, and undetected baryons trace non baryonic matter therein, two main consequences arise, namely (i) velocity dispersions along the line of sight are lower than in absence of undetected baryons, and (ii) dark matter haloes are dynamically “hotter” than stellar ellipsoids, the transition occurring when the amount of undetected baryons is about one and a half times that of the stellar subsystem. In this view, both the observation that the temperature of the extended hot gas exceeds the central stellar temperature, and the fact that the non baryonic matter is dynamically “hotter” than the stars, are a reflection of the presence of

undetected baryons, which trace the dark halo and are about twice as massive as the stellar ellipsoid.

Key words. Cosmology: dark matter - galaxies: haloes.

1. Introduction

According to standard CDM or Λ CDM cosmological scenarios, large-scale celestial objects such as galaxies and clusters of galaxies, are made of at least two components: one, baryonic and more concentrated, embedded within one other, non baryonic and dissipationless, usually named dark matter halo. After a wide number of both analytical and numerical studies (e.g., Cole & Lacey 1996; Navarro et al. 1995, 1996, 1997; Moore et al. 1998, 1999; Fukushige & Makino 2001; Klypin et al. 2001), it has been realized that dark matter haloes which virialize from hierarchical clustering show universal density profiles, $\rho = \rho(r; \rho^\dagger, r^\dagger)$, where ρ^\dagger is a scaling density and r^\dagger is a scaling radius. In this view, smaller haloes formed first from initial density perturbations and then merged with each other, or were tidally disrupted from previously formed mergers, to become larger haloes.

The density profile is (i) self-similar, in the sense that it has the same expression, independent of time (e.g., Fukushige & Makino 2001), and (ii) universal, in the sense that it has the same expression, independent of halo mass, initial density perturbation spectrum, or value of cosmological parameters (e.g., Navarro et al. 1997; Fukushige & Makino 2001). A satisfactory fit to the results of numerical simulations is the family of density profiles (e.g., Hernquist 1990; Zhao 1996):

$$\rho\left(\frac{r}{r^\dagger}\right) = \frac{\rho^\dagger}{(r/r^\dagger)^\gamma [1 + (r/r^\dagger)^\alpha]^\chi} \quad ; \quad \chi = \frac{\beta - \gamma}{\alpha} \quad ; \quad (1)$$

for a suitable choice of exponents, α , β , and γ .

This family includes both cuspy profiles first proposed by Navarro et al. (1995, 1996, 1997), $(\alpha, \beta, \gamma) = (1, 3, 1)$, and the so called modified isothermal profile, $(\alpha, \beta, \gamma) = (2, 2, 0)$, which is the most widely used model for the halo density distribution in analyses of observed rotation curves. It also includes the perfect ellipsoid (e.g., de Zeeuw 1985), $(\alpha, \beta, \gamma) = (2, 4, 0)$, which is the sole (known) ellipsoidal density profile where a test particle admits three global integrals of motion. Finally, it includes the Hernquist (1990) density profile, $(\alpha, \beta, \gamma) = (1, 4, 1)$, which closely approximates the de Vaucouleurs $r^{1/4}$ law for elliptical galaxies. In dealing with the formation of dark matter haloes from hierarchical clustering in both CDM and Λ CDM scenarios, recent high-resolution simulations allow $(\alpha, \beta, \gamma) = (3/2, 3, 3/2)$, as a best fit (e.g., Ghigna et al. 2000; Fukushige & Makino 2001; Klypin et al. 2001), as first advocated by Moore et al. (1998, 1999)¹.

Send offprint requests to: R. Caimmi

¹ More precisely, an exponent $\alpha = 1.4$ was derived by Moore et al. (1998), while the value $\alpha = 1.5$ was established by Moore et al. (1999).

Though Eq. (1) implies null density at infinite radius, the mass distribution has necessarily to be truncated for two types of reasons. First, the presence of neighbouring systems makes the tidal radius an upper limit. On the other hand, isolated, over-dense objects cannot extend outside the Hubble sphere of equal mass. Second, the total mass, deduced from Eq. (1) for an infinitely extended configuration, is divergent, at least with regard to the special choices of exponents, $(\alpha, \beta, \gamma) = (1, 3, 1)$, hereafter quoted as NFW density profile, and $(\alpha, \beta, \gamma) = (3/2, 3, 3/2)$, hereafter quoted as MOA density profile. The region enclosed within the truncation boundary has to be intended as representative of the quasi static halo interior, leaving aside the surrounding material which is still infalling. It is worth remembering that the total mass can be finite even for an infinitely extended configuration, provided the related density profile is sufficiently steep e.g., $(\alpha, \beta, \gamma) = (1, 4, 1)$, hereafter quoted as H density profile.

In dealing with numerical simulations of dark matter haloes, it is usual to take into consideration spherically averaged density profiles (e.g., Cole & Lacey 1996; Navarro et al. 1997; Fukushige & Makino 2001; Klypin et al. 2001), or in other terms spherical isopycnic (i.e. of equal density) surfaces. On the other hand, spin growth by tidal interactions with neighbouring objects, in expanding density perturbations, demands ellipsoidally averaged density profiles (e.g., Doroshkevich 1970; White 1984; Maller et al. 2002; Jing & Suto 2002), or in other terms ellipsoidal isopycnic surfaces. As a best compromise between intrinsic simplicity and unavoidable necessity, our attention will be devoted to homeoidally striated configurations, i.e. the isopycnic surfaces are similar and similarly placed ellipsoids.

Galaxies and cluster of galaxies may safely be idealized as two subsystems which link only via gravitational interaction, in such a way that each component is distorted by the tidal potential induced by the other. Then the application of the virial theorem in tensor form may be performed either to the whole system or to each subsystem separately. Towards this aim, the explicit expression of the potential-energy tensors are needed. Though some results are available in literature (e.g., Brosche et al. 1983; Caimmi & Secco 1992; Caimmi 1993, 1995), the related density profiles exhibit no central divergence, or “cusp”, in contradiction with Eq. (1) when $\gamma > 0$.

The present attempt aims mainly to (i) formulate a general theory of homeoidally striated density profiles with a central cusp; (ii) devote further investigation to a few special cases which are consistent with the results of both observations and simulations related to galaxies and cluster of galaxies; (iii) apply to galaxies, as the analogon to clusters of galaxies performed in an earlier paper (Caimmi, 2002).

The current paper is organized in the following way. The general theory of homeoidally striated, density profiles with a central cusp, is performed in Sect. 2. The general results are particularized to NFW, MOA, and H density profiles, which provide good fits to the results from both observations (e.g., Geller et al. 1999; Rines et al. 2001) and numerical

simulations (e.g., Klypin et al. 2001), in Sect. 3. An application to elliptical galaxies is performed in Sect. 4. Finally, some concluding remarks are reported in Sect. 5. Further details on fitting simulated and theoretical, self-similar, universal density profiles, are illustrated in the Appendix.

2. Homeoidally striated density profiles with a central cusp

A general theory of homeoidally striated density profiles, where no divergence in the density occurs, has been developed in an earlier approach (Caimmi 1993, hereafter quoted as C93). Here we take into consideration a more general approach, where a central cusp may occur. The isopycnic surfaces are defined by the following law:

$$\rho = \rho^\dagger f(\xi) \quad ; \quad f(1) = 1 \quad ; \quad (2a)$$

$$\xi^2 = \sum_{\ell=1}^3 \frac{x_\ell^2}{(a_\ell^\dagger)^2} \quad ; \quad 0 \leq \xi \leq \Xi \quad ; \quad (2b)$$

where $\rho^\dagger = \rho(1)$, a_ℓ^\dagger , are the density and the semiaxes, respectively, of a reference isopycnic surface, and Ξ corresponds to the truncation isopycnic surface, related to semiaxes a_ℓ .

Then the scaling density, ρ^\dagger , and the scaling radius (related to the reference isopycnic surface), r^\dagger , correspond to a single boundary, which allows the description of cuspy density profiles. On the other hand, centrally regular density profiles defined in C93 fail in this respect, as the scaling density coincides with the central density and the scaling radius attains the external surface.

The assumption that the system is homeoidally striated (Roberts 1962) implies the following properties (e.g., C93):

$$\xi = \frac{a'_p}{a_p^\dagger} \quad ; \quad d\xi = \frac{da'_p}{a_p^\dagger} \quad ; \quad p = 1, 2, 3 \quad ; \quad (3a)$$

$$\frac{\partial \xi}{\partial x_p} = \frac{x_p}{\xi (a_p^\dagger)^2} \quad ; \quad p = 1, 2, 3 \quad ; \quad \sum_{\ell=1}^3 x_\ell \frac{\partial \xi}{\partial x_\ell} = \xi \quad ; \quad (3b)$$

where a'_p are the semiaxes of the isopycnic surface under consideration.

The generic point on an isopycnic surface obeys the equation:

$$\frac{x_1^2}{a_1'^2} + \frac{x_2^2}{a_2'^2} + \frac{x_3^2}{a_3'^2} = \frac{r^2 \sin^2 \theta \cos^2 \phi}{a_1'^2} + \frac{r^2 \sin^2 \theta \sin^2 \phi}{a_2'^2} + \frac{r^2 \cos^2 \theta}{a_3'^2} = 1 \quad ; \quad (4)$$

where $P(x_1, x_2, x_3) \equiv P(r, \theta, \phi)$. Taking spherical coordinates into consideration, Eq. (4) may be cast into the equivalent form:

$$\begin{aligned} & \frac{r^2}{(r^\dagger)^2} \frac{(r^\dagger)^2}{(a_1^\dagger)^2} \frac{(a_1^\dagger)^2}{a_1'^2} \sin^2 \theta \cos^2 \phi + \frac{r^2}{(r^\dagger)^2} \frac{(r^\dagger)^2}{(a_2^\dagger)^2} \frac{(a_2^\dagger)^2}{a_2'^2} \sin^2 \theta \sin^2 \phi + \frac{r^2}{(r^\dagger)^2} \frac{(r^\dagger)^2}{(a_3^\dagger)^2} \frac{(a_3^\dagger)^2}{a_3'^2} \cos^2 \theta = \\ & \frac{r^2}{(r^\dagger)^2} \frac{1}{\xi^2} \left[\frac{(r^\dagger)^2}{(a_1^\dagger)^2} \sin^2 \theta \cos^2 \phi + \frac{(r^\dagger)^2}{(a_2^\dagger)^2} \sin^2 \theta \sin^2 \phi + \frac{(r^\dagger)^2}{(a_3^\dagger)^2} \cos^2 \theta \right] = 1 \quad ; \end{aligned} \quad (5)$$

where r^\dagger is the radial coordinate of the point, $P^\dagger(r^\dagger, \theta, \phi)$, on the reference isopycnic surface. Accordingly, the expression within brackets in Eq. (5) makes the particularization

of Eq. (4) to the reference isopycnic surface, and necessarily equals unity. Then Eq. (5) reduces to:

$$\xi = \frac{r}{r^\dagger} ; \quad (6)$$

regardless of the radial direction. The particularization of Eq. (6) to the truncation boundary yields:

$$\Xi = \frac{R}{r^\dagger} ; \quad (7)$$

regardless of the radial direction.

The above results may be summarized as follows. Given a homeoidally striated density profile, and two generic points with coinciding angular coordinates, $P(r, \theta, \phi)$ and $P^\dagger(r^\dagger, \theta, \phi)$, placed on two isopycnic surfaces, $r(\theta, \phi)$ and $r^\dagger(\theta, \phi)$, the ratio of the radial coordinates, $\xi = r/r^\dagger$, does not depend on the radial direction. Then Eqs. (3a) follow from (6) as special cases.

2.1. Mass and inertia tensor

The volume, the mass, and the inertia tensor of an infinitely thin homeoid bounded by isopycnic surfaces, may be expressed as (e.g., C93):

$$dS' = 4\pi a_1^\dagger a_2^\dagger a_3^\dagger \xi^2 d\xi = 3S^\dagger \xi^2 d\xi ; \quad (8)$$

$$dM' = 4\pi \rho^\dagger a_1^\dagger a_2^\dagger a_3^\dagger f(\xi) \xi^2 d\xi = 3M^\dagger f(\xi) \xi^2 d\xi ; \quad (9)$$

$$dI'_{pq} = \frac{4\pi}{3} \rho^\dagger \delta_{pq} (a_p^\dagger)^3 a_q^\dagger a_r^\dagger f(\xi) \xi^4 d\xi = \delta_{pq} M^\dagger (a_p^\dagger)^2 f(\xi) \xi^4 d\xi ; \quad (10)$$

where S^\dagger and M^\dagger are the volume and mass, respectively, of a homogeneous ellipsoid, bounded by the reference isopycnic surface, and with the same density, ρ^\dagger , as at the reference isopycnic surface; and δ_{pq} is the Kronecker symbol.

Let us define, according to Roberts (1962):

$$F(\xi) = 2 \int_\xi^{\Xi} f(\xi') \xi' d\xi' ; \quad (11)$$

from which the following relations are easily derived:

$$F(\Xi) = 0 ; \quad \frac{dF}{d\xi} = -2\xi f(\xi) ; \quad (12)$$

an integration by parts of Eq. (11) shows that:

$$\int_0^\Xi f(\xi) \xi^n d\xi = \frac{n-1}{2} \int_0^\Xi F(\xi) \xi^{n-2} d\xi ; \quad n > 1 ; \quad (13)$$

which allows the calculation of the total mass as:

$$M = \nu_{mas} M^\dagger ; \quad (14a)$$

$$\nu_{mas} = \frac{3}{2} \int_0^\Xi F(\xi) d\xi ; \quad (14b)$$

$$M^\dagger = \frac{4\pi}{3} \rho^\dagger a_1^\dagger a_2^\dagger a_3^\dagger ; \quad (14c)$$

and the inertia tensor as:

$$I_{pq} = \delta_{pq} \nu_{inr} M^\dagger (a_p^\dagger)^2 ; \quad (15a)$$

$$\nu_{inr} = \frac{3}{2} \int_0^\Xi F(\xi) \xi^2 d\xi ; \quad (15b)$$

where the coefficients, ν_{mas} and ν_{inr} , are shape-independent and may be conceived as profile factors (C93).

The mass enclosed within a selected isopycnic surface, $\rho = \rho^\dagger f(\xi)$, $0 \leq \xi \leq \Xi$, is obtained by integration of Eq. (9). The result is:

$$M(\xi) = 3M^\dagger \int_0^\xi f(\xi') \xi'^2 d\xi' ; \quad (16)$$

and the related mean density is:

$$\bar{\rho}(\xi) = \frac{M(\xi)}{S(\xi)} = 3\rho^\dagger \frac{1}{\xi^3} \int_0^\xi f(\xi') \xi'^2 d\xi' ; \quad (17)$$

where Eqs. (8) and (16) have been taken into consideration.

2.2. Tensor potential and self-energy tensor

The tensor potential induced by an infinitely thin homeoid bounded by isopycnic surfaces, on a generic point placed at its interior, is (e.g., C93):

$$d\mathcal{V}_{pq}^{(int)} = 2\pi G \delta_{pq} \rho^\dagger (a_p^\dagger)^2 A_p f(\xi) \xi d\xi ; \quad (18)$$

where G is the constant of gravitation, $p = 1, 2, 3$, $q = 1, 2, 3$, and A_p are shape factors which, *ipso facto*, depend on the axis ratios only (e.g., Caimmi 1992; therein defined as $\hat{\alpha}_p$).

The tensor potential induced by all the homeoids enclosing a given point, on that point, is (e.g., C93):

$$\mathcal{V}_{pq}^{(int)} = \pi G \delta_{pq} \rho^\dagger (a_p^\dagger)^2 A_p F(\xi_p) ; \quad (19)$$

where ξ_p denotes the isopycnic surface passing through the point, and Eq. (11) has been used.

The interaction-energy tensor related to an infinitely thin homeoid bounded by isopycnic surfaces, embedded into another infinitely thin homeoid of the same kind, is (C93):

$$d^2(E_{int})_{pq} = -4\pi^2 G \delta_{pq} (\rho^\dagger)^2 (a_p^\dagger)^3 a_s^\dagger a_r^\dagger A_p f(\xi) \xi f(\xi') \xi'^2 d\xi d\xi' ; \quad (20)$$

if the two boundaries coincide, $\xi = \xi'$ and $d^2(E_{int})_{pq}(\xi = \xi') = d^2(E_{sel})_{pq}$, i.e. the interaction-energy tensor reduces to the self-energy tensor. Bearing in mind that Eq. (20) remains unchanged by replacing ξ' with ξ and vice versa, the self-energy tensor of the whole mass distribution may be written as $(E_{sel})_{pq} = 2 \int \int_S d^2(E_{int})_{pq}$; the result is

(e.g., C93):

$$(E_{sel})_{pq} = -\delta_{pq}\nu_{sel}\frac{G(M^\dagger)^2}{a_1^\dagger}\epsilon_{p2}\epsilon_{p3}A_p ; \quad (21a)$$

$$\nu_{sel} = \frac{9}{16}\int_0^\Xi F^2(\xi) d\xi ; \quad (21b)$$

$$\epsilon_{pq} = \frac{a_p}{a_q} ; \quad (21c)$$

where ν_{sel} is a profile factor, i.e. shape-independent, and ϵ_{pq} are axis ratios.

Let $P(r, \theta, \phi)$ be a generic point on an isopycnic surface, $\rho = \rho^\dagger f(\xi)$, $0 \leq \xi \leq \Xi$. A test particle at P is centrifugally supported with respect to the centre of mass, provided the following relation holds:

$$\frac{GM(\xi)\eta(r, \theta, \phi)}{r^2} = \frac{v_{eq}^2(r, \theta, \phi)}{r} ; \quad (22)$$

where η represents the deviation from the spherical limit and/or the Roche-like (i.e. a mass point surrounded by a massless, ellipsoidal atmosphere) limit, and v_{eq} is the rotational velocity with respect to the centre of mass. Due to Newton's theorem, a generic homeoid bounded by isopycnic surfaces, related to $\xi' > \xi$, $\xi'' > \xi$, exerts no action on P (e.g., Chandrasekhar 1969, Chap. 3, §17). In this respect, only the mass, $M(\xi)$, enclosed within the isopycnic surface under consideration, is effective.

The particularization of Eq. (22) to a point, $P^\dagger(r^\dagger, \theta, \phi)$, on the reference isopycnic surface, reads:

$$\frac{GM(1)\eta(r^\dagger, \theta, \phi)}{(r^\dagger)^2} = \frac{v_{eq}^2(r^\dagger, \theta, \phi)}{r^\dagger} ; \quad (23)$$

and the combination of Eqs. (6), (22) and (23) yields:

$$\frac{v_{eq}^2(r, \theta, \phi)}{v_{eq}^2(r^\dagger, \theta, \phi)} = \frac{1}{\xi} \frac{M(\xi)}{M(1)} \frac{\eta(r, \theta, \phi)}{\eta(r^\dagger, \theta, \phi)} ; \quad (24)$$

provided the point on the generic isopycnic surface, $P(r, \theta, \phi)$, and the point on the reference isopycnic surface, $P^\dagger(r^\dagger, \theta, \phi)$, are aligned along the same radial direction.

It is worth noting that the density profiles of interest, i.e. decreasing from the centre to the boundary, lie between two extreme situations: the homogeneous limit and the Roche-like limit, where the ratio, $\eta(r, \theta, \phi)/\eta(r^\dagger, \theta, \phi)$, reduces to unity in both cases.

If the angular coordinates are specified, Eq. (24) takes the simpler form:

$$\frac{v_{eq}^2(\xi)}{(v_{eq}^\dagger)^2} = \frac{1}{\xi} \frac{M(\xi)}{M(1)} \frac{\eta(\xi)}{\eta^\dagger} ; \quad (25a)$$

$$v_{eq}^\dagger = v_{eq}(r^\dagger, \theta, \phi) ; \quad \eta^\dagger = \eta(r^\dagger, \theta, \phi) ; \quad (25b)$$

where it is intended that the velocity profile corresponds to the $(r^\dagger, \theta, \phi)$ direction.

2.3. Angular-momentum vector and rotational-energy tensor

In dealing with angular momentum and rotational energy, the knowledge of the rotational velocity field is needed. Let us define the angular-momentum vector and the rotational-energy tensor, respectively, as:

$$J_p = \int \int \int_S \Omega_p d^3 I_{\ell\ell} + \int \int \int_S \Omega_p d^3 I_{qq} - \int \int \int_S \Omega_\ell d^3 I_{p\ell} + \int \int \int_S \Omega_q d^3 I_{pq} ; \quad p \neq \ell ; \quad q \neq \ell ; \quad (26)$$

$$2(E_{rot})_{pq} = \int \int \int_S \Omega_p \Omega_q d^3 I_{\ell\ell} - \int \int \int_S \Omega_\ell \Omega_p d^3 I_{q\ell} - \int \int \int_S \Omega_q \Omega_\ell d^3 I_{\ell p} + \int \int \int_S \Omega_\ell^2 d^3 I_{pq} ; \quad p \neq \ell ; \quad q \neq \ell ; \quad (27)$$

where $\mathbf{\Omega} = (\Omega_1, \Omega_2, \Omega_3)$ is the angular-velocity vector, and $d^3 I_{pq}$ is the inertia tensor, related to a generic, infinitesimal mass element.

The symmetry of the tensors under consideration, due to Eq. (15a), together with the conditions, $p \neq \ell$, $q \neq \ell$, implies the following values for the index, ℓ :

$$\ell = 1 , \quad p \vee q = 2 , \quad p \neq 1 \ \& \ q \neq 1 ; \quad (28a)$$

$$\ell = 2 , \quad p \vee q = 3 , \quad p \neq 2 \ \& \ q \neq 2 ; \quad (28b)$$

$$\ell = 3 , \quad p \vee q = 1 , \quad p \neq 3 \ \& \ q \neq 3 ; \quad (28c)$$

where \vee and $\&$ are the semantic symbol of disjunction, “or”, and conjunction, “and”, respectively.

The preservation of ellipsoidal shape imposes severe constraints on the rotational velocity field. Leaving an exhaustive investigation to more refined approaches, our attention will be limited to a restricted number of special cases, namely: (i) rigid rotation about a principal axis, and (ii) differential rotation about a symmetry axis, in connection with a particular class of velocity distributions. By “rotation” it is intended, of course, circular rotation. Accordingly, $\mathbf{\Omega} = (\delta_{1s}\Omega_1, \delta_{2s}\Omega_2, \delta_{3s}\Omega_3)$ provided x_s is assumed as rotation axis.

The angular momentum and the rotational energy, related to axis x_s , are:

$$J(s) = J_s = \int \int \int_S \Omega_s d^3 I_{pp} + \int \int \int_S \Omega_s d^3 I_{qq} ; \quad p \neq q \neq s ; \quad (29)$$

$$E_{rot}(s) = (E_{rot})_s = (E_{rot})_{pp} + (E_{rot})_{qq} = \int \int \int_S \Omega_s^2 d^3 I_{pp} + \int \int \int_S \Omega_s^2 d^3 I_{qq} ; \quad p \neq q \neq s ; \quad (30)$$

where $s = 3$ is usually assumed, and then $p = 1$, $q = 2$, or vice versa. For the sake of brevity, from this point on J_s and $(E_{rot})_s$ shall be denoted as J and E_{rot} , respectively.

In the special case of rigid rotation about a principal axis, Eq. (27), by use of (15a), reads:

$$(E_{rot})_{pq} = \frac{1}{2} I_{pq} \Omega_r^2 = \frac{1}{2} \delta_{pq} (1 - \delta_{pr}) \nu_{inr} M^\dagger (a_p^\dagger)^2 \Omega_r^2 = \frac{1}{2} \delta_{pq} (1 - \delta_{pr}) \nu_{inr} M^\dagger (v_{rot}^\dagger)_p^2 ; \quad (31)$$

and Eqs. (29), (30), taking $s = 3$, read:

$$J = (I_{11} + I_{22})\Omega = \nu_{inr} M^\dagger a_1^\dagger (1 + \epsilon_{21}^2) v_{rot}^\dagger ; \quad (32)$$

$$E_{rot} = \frac{1}{2} \nu_{inr} M^\dagger (1 + \epsilon_{21}^2) (v_{rot}^\dagger)^2 ; \quad (33)$$

where $\mathbf{v}_{rot} = \boldsymbol{\Omega} \times \mathbf{r}$ and $v_{rot}^\dagger = (v_{rot}^\dagger)_1$ is the rotational velocity at the end of the major semiaxis, a_1^\dagger , with regard to the reference isopycnic surface.

In the special case of differential rotation about a symmetry axis, our attention shall be restricted to (rotational) velocity distributions which satisfy the counterpart of Eq. (6), namely:

$$\frac{v_{rot}(r, \theta)}{v_{rot}(r^\dagger, \theta)} = \frac{v_{rot}(a', 0)}{v_{rot}(a^\dagger, 0)} ; \quad (34)$$

where (r, θ) , (r^\dagger, θ) , represent a point on a generic and reference isopycnic surface, respectively, along the same radial direction, and $(a', 0)$, $(a^\dagger, 0)$, represent the end of the corresponding, major semiaxes. Due to Eqs. (3a) and (6), Eq. (34) may be written under the equivalent form:

$$\frac{\Omega(r, \theta)}{\Omega(r^\dagger, \theta)} = \frac{\Omega(a', 0)}{\Omega(a^\dagger, 0)} ; \quad (35)$$

where rotational velocity is replaced by angular velocity. It is worth noting that, in particular, either rotational or angular velocity is allowed to be constant everywhere.

Both rotational and angular velocity are independent of the longitudinal angle, ϕ , according to Eqs. (34) and (35), respectively. It follows that sections of infinitely thin, homogeneous homeoids, by infinitely thin layers normal to the symmetry axis, do rotate rigidly. The related volume, inertia tensor, angular-momentum vector, rotational-energy tensor, are (e.g., Caimmi & Secco 1993):

$$d^2 S = \frac{2\pi\epsilon^3 (a^\dagger)^3 \xi^2 \sin \theta d\xi d\theta}{(\cos^2 \theta + \epsilon^2 \sin^2 \theta)^{3/2}} ; \quad (36)$$

$$d^2 I_{1q} = d^2 I_{2q} = \frac{3}{4} \delta_{1q} M^\dagger (a^\dagger)^2 \epsilon^4 f(\xi) \xi^4 \frac{\sin^3 \theta d\xi d\theta}{(\cos^2 \theta + \epsilon^2 \sin^2 \theta)^{5/2}} ; \quad (37a)$$

$$d^2 I_{3q} = \frac{3}{2} \delta_{3q} M^\dagger (a^\dagger)^2 \epsilon^4 f(\xi) \xi^4 \frac{\sin \theta \cos^2 \theta d\xi d\theta}{(\cos^2 \theta + \epsilon^2 \sin^2 \theta)^{5/2}} ; \quad (37b)$$

$$d^2 J = \Omega(\xi, \theta) [d^2 I_{11} + d^2 I_{22}] ; \quad (38)$$

$$d^2 (E_{rot})_{pq} = \frac{1}{2} \delta_{pq} (1 - \delta_{p3}) \Omega^2(\xi, \theta) d^2 I_{pq} ; \quad (39)$$

where, due to axial symmetry, $a_1^\dagger = a_2^\dagger = a^\dagger$, $\epsilon_{21} = 1$, $\epsilon_{31} = \epsilon$, and θ is the azimuthal angle. The angular-momentum vector and the rotational-energy tensor, by use of Eqs. (14c) and (35)-(39), take the equivalent form:

$$d^2 J = \frac{3}{2} M^\dagger (a^\dagger)^2 \epsilon^4 f(\xi) \xi^4 \Omega(\xi, 0) \frac{\Omega(1, \theta)}{\Omega(1, 0)} \frac{\sin^3 \theta d\xi d\theta}{(\cos^2 \theta + \epsilon^2 \sin^2 \theta)^{5/2}} ; \quad (40)$$

$$d^2 (E_{rot})_{pq} = \frac{3}{8} \delta_{pq} (1 - \delta_{p3}) M^\dagger (a^\dagger)^2 \epsilon^4 f(\xi) \xi^4 \Omega^2(\xi, 0) \frac{\Omega^2(1, \theta)}{\Omega^2(1, 0)} \frac{\sin^3 \theta d\xi d\theta}{(\cos^2 \theta + \epsilon^2 \sin^2 \theta)^{5/2}} ; \quad (41)$$

where, due to Eqs. (34), (35), the ratios, $v_{rot}(1, \theta)/v_{rot}(1, 0)$, $\Omega(1, \theta)/\Omega(1, 0)$, only depend on the azimuthal angle.

An integration over the whole, homogeneous, infinitely thin homeoid yields:

$$dJ = 2\eta_{anm} M^\dagger (a^\dagger)^2 \Omega(\xi, 0) f(\xi) \xi^4 d\xi ; \quad (42)$$

$$\eta_{anm} = \frac{3}{4} \epsilon^4 \int_{-\pi/2}^{+\pi/2} \frac{\Omega(1, \theta)}{\Omega(1, 0)} \frac{\sin^3 \theta d\theta}{(\cos^2 \theta + \epsilon^2 \sin^2 \theta)^{5/2}} ; \quad (43)$$

$$d(E_{rot})_{pq} = \delta_{pq} (1 - \delta_{p3}) \eta_{rot} M^\dagger (a^\dagger)^2 \Omega^2(\xi, 0) f(\xi) \xi^4 d\xi ; \quad (44)$$

$$\eta_{rot} = \frac{3}{8} \epsilon^4 \int_{-\pi/2}^{+\pi/2} \frac{\Omega^2(1, \theta)}{\Omega^2(1, 0)} \frac{\sin^3 \theta d\theta}{(\cos^2 \theta + \epsilon^2 \sin^2 \theta)^{5/2}} ; \quad (45)$$

finally, an integration over the whole system yields, for the angular-momentum vector:

$$J = 2\eta_{anm} \nu_{anm} M^\dagger v_{rot}^\dagger a^\dagger ; \quad (46a)$$

$$\nu_{anm} = \int_0^\Xi \frac{\Omega(\xi, 0)}{\Omega(1, 0)} f(\xi) \xi^4 d\xi ; \quad (46b)$$

and for the rotational-energy tensor:

$$(E_{rot})_{pq} = \delta_{pq} (1 - \delta_{p3}) \eta_{rot} \nu_{rot} M^\dagger (v_{rot}^\dagger)^2 ; \quad (47a)$$

$$\nu_{rot} = \int_0^\Xi \frac{\Omega^2(\xi, 0)}{\Omega^2(1, 0)} f(\xi) \xi^4 d\xi ; \quad (47b)$$

it is apparent that η_{anm} , η_{rot} , depend on the integration over the boundary and may be thought of as shape factors, even if they may also be shape-independent, whereas ν_{anm} , ν_{rot} , are genuine profile factors.

The special case of rigid rotation, implies the relation:

$$\frac{\Omega(\xi, \theta)}{\Omega(\xi, 0)} = 1 ; \quad (48)$$

the special case of constant rotational velocity on the equatorial plane, implies the relation:

$$\frac{\Omega(\xi, 0)}{\Omega(1, 0)} = \frac{a^\dagger}{a'} = \frac{1}{\xi} ; \quad (49)$$

the special case of constant rotational velocity everywhere, implies the relation:

$$\frac{\Omega(\xi, \theta)}{\Omega(\xi, 0)} = \frac{a'}{r \sin \theta} = \frac{(\cos^2 \theta + \epsilon^2 \sin^2 \theta)^{1/2}}{\epsilon \sin \theta} ; \quad (50)$$

the corresponding values of the shape parameters, η_{anm} , η_{rot} , and profile parameters, ν_{anm} , ν_{rot} , are listed in Table 1.

2.4. Other potential-energy tensors for subsystems with similar boundaries

The above results are related to a single subsystem: strictly speaking, all the quantities discussed in the last Section should be labelled by the index, u , in connection with u th subsystem (e.g., Caimmi & Secco 1992), but it has been omitted for the sake of clarity. On the other hand, the formulation of the interaction-energy tensor and the tidal-energy

case	RR	RC	CV
isopycnic surface	$\frac{\Omega(\xi, \theta)}{\Omega(\xi, 0)} = 1$	$\frac{\Omega(\xi, \theta)}{\Omega(\xi, 0)} = 1$	$\frac{v_{rot}(\xi, \theta)}{v_{rot}(\xi, 0)} = 1$
equatorial plane	$\frac{\Omega(\xi, 0)}{\Omega(1, 0)} = 1$	$\frac{v_{rot}(\xi, 0)}{v_{rot}(1, 0)} = 1$	$\frac{v_{rot}(\xi, 0)}{v_{rot}(1, 0)} = 1$
η_{anm}	1	1	$3\pi/8$
η_{rot}	1/2	1/2	3/4
ν_{anm}	ν_{inr}	$\int_0^\Xi f(\xi) \xi^3 d\xi$	$\int_0^\Xi f(\xi) \xi^3 d\xi$
ν_{rot}	ν_{inr}	$\nu_{mas}/3$	$\nu_{mas}/3$

Table 1. Values of the shape parameters, η_{anm} , η_{rot} , and profile parameters, ν_{anm} , ν_{rot} , related to (i) homeoidally striated ellipsoids in rigid rotation about a principal axis (RR), and (ii) homeoidally striated spheroids in differential rotation about the symmetry axis where the isopycnic surfaces are: either in rigid rotation and the rotational velocity on the equatorial plane is constant (RC), or in cylindric rotation and the rotational velocity is constant everywhere (CV).

tensor necessarily involves at least two components. The related calculations turn out to be very difficult in the general case, and for this reason our attention shall be limited to subsystems with similar boundaries, and homeoidally striated density profiles with a central cusp.

Using a similar procedure as in C93, where no (central) cusp occurs in density profiles, but bearing in mind that the scaled density and the scaled radius have a different definition, yields the expression of the interaction-energy tensors:

$$[(E_{ij})_{int}]_{pq} = -\delta_{pq} \frac{G(M_i^\dagger)^2}{(a_i^\dagger)_1} (\nu_{ij})_{int} \epsilon_{p2} \epsilon_{p3} A_p ; \quad (51a)$$

$$(\nu_{ij})_{int} = -\frac{9}{16} m^\dagger \left[w^{(int)}(\Xi_i/y^\dagger) + w^{(ext)}(\Xi_i/y^\dagger) \right] ; \quad (51b)$$

$$[(E_{ji})_{int}]_{pq} = [(E_{ij})_{int}]_{pq} ; \quad (51c)$$

the expression of the tidal-energy tensors:

$$[(E_{ij})_{tid}]_{pq} = -\delta_{pq} \frac{G(M_i^\dagger)^2}{(a_i^\dagger)_1} (\nu_{ij})_{tid} \epsilon_{p2} \epsilon_{p3} A_p ; \quad (52a)$$

$$(\nu_{ij})_{tid} = -\frac{9}{8} m^\dagger w^{(ext)}(\Xi_i/y^\dagger) ; \quad (52b)$$

$$[(E_{ji})_{tid}]_{pq} = -\delta_{pq} \frac{G(M_j^\dagger)^2}{(a_j^\dagger)_1} (\nu_{ji})_{tid} \epsilon_{p2} \epsilon_{p3} A_p ; \quad (52c)$$

$$(\nu_{ji})_{tid} = -\frac{9}{8} \frac{y^\dagger}{m^\dagger} w^{(int)}(\Xi_i/y^\dagger) ; \quad (52d)$$

and the expression of the residual-energy tensors:

$$[(E_{ij})_{res}]_{pq} = -\delta_{pq} \frac{G(M_i^\dagger)^2}{(a_i^\dagger)_1} (\nu_{ij})_{res} \epsilon_{p2} \epsilon_{p3} A_p ; \quad (53a)$$

$$(\nu_{ij})_{res} = -\frac{9}{16} m^\dagger \left[w^{(ext)}(\Xi_i/y^\dagger) - w^{(int)}(\Xi_i/y^\dagger) \right] ; \quad (53b)$$

$$[(E_{ji})_{res}]_{pq} = -[(E_{ij})_{res}]_{pq} ; \quad (53c)$$

where the functions, $w^{(int)}$ and $w^{(ext)}$, are defined as:

$$w^{(int)}(\eta) = \int_0^\eta F_j(\xi_j) \frac{dF_i}{d\xi_j} \xi_j d\xi_j \quad ; \quad (54a)$$

$$w^{(ext)}(\eta) = \int_0^\eta F_i(\xi_i) \frac{dF_j}{d\xi_j} \xi_j d\xi_j \quad ; \quad (54b)$$

the parameters, m^\dagger and y^\dagger , are defined as:

$$m^\dagger = \frac{M_j^\dagger}{M_i^\dagger} \quad ; \quad y^\dagger = \frac{r_j^\dagger}{r_i^\dagger} \quad ; \quad (55)$$

and the combination of Eqs. (7) and (55) yields:

$$\frac{\Xi_j}{\Xi_i} = \frac{y}{y^\dagger} \quad ; \quad y = \frac{R_j}{R_i} \quad ; \quad (56)$$

finally, the virial-energy tensors (e.g., Caimmi & Secco 2002), $[(E_{uv})_{vir}]_{pq} = [(E_u)_{sel}]_{pq} + [(E_{uv})_{tid}]_{pq}$, take the expression:

$$[(E_{uv})_{vir}]_{pq} = -\delta_{pq} \frac{G(M_u^\dagger)^2}{(a_u^\dagger)_1} (\nu_{uv})_{vir} \epsilon_{p2} \epsilon_{p3} A_p \quad ; \quad (57a)$$

$$(\nu_{uv})_{vir} = (\nu_u)_{sel} + (\nu_{uv})_{tid} \quad ; \quad u = i, j \quad ; \quad v = j, i \quad ; \quad (57b)$$

in conclusion, Eqs.(51)-(57) allow the calculation of potential-energy tensors for homeoidally striated density profiles with a central cusp, related to two subsystems with similar and similarly placed boundaries.

3. Special cases

The physical parameters related to the density profiles expressed by Eq. (1), and investigated in Sect. 2, may be explicitly calculated, provided the exponents, (α, β, γ) , are specified. Our attention shall be limited to two special cases, which are consistent with high-resolution simulations of cold dark matter haloes (e.g., Klypin et al. 2001): NFW, first recognized by Navarro et al. (1995, 1996, 1997), and MOA, first recognized by Moore et al. (1998, 1999). As far as we know, no method has been clearly outlined for fitting simulated and theoretical, self-similar, universal density profiles. A possible procedure is sketched out in Appendix A for a single matter distribution which obeys Eq. (1), and in Appendix B for two different mass distributions which obey Eq. (1). In addition, a third density profile will be taken into consideration, which is consistent (together with NFW) with observations (e.g., Geller et al. 1999; Rines et al. 2001; Holley-Bockelmann et al. 2001): H, first proposed by Hernquist (1990).

With regard to the shape parameters, η_{anm} , η_{rot} , and the profile parameters, ν_{anm} , ν_{rot} , it is worth remembering that they are listed in Table 1 for the velocity profiles discussed in Sect. 2, where differential rotation corresponds to axisymmetric configurations with constant rotational velocity, either on the equatorial plane or everywhere.

3.1. The NFW density profile

The NFW density profile corresponds to the choice of exponents $(\alpha, \beta, \gamma) = (1, 3, 1)$ in Eq. (1). Accordingly, Eq. (2a) reads:

$$\rho(\xi) = \rho^\dagger f(\xi) \quad ; \quad f(\xi) = \frac{4}{\xi(1+\xi)^2} \quad ; \quad (58)$$

and Eq. (11), after integration, takes the explicit expression:

$$F(\xi) = \frac{8}{1+\xi} - \frac{8}{1+\Xi} \quad ; \quad (59)$$

where the truncated, scaled radius, defined by Eq. (7), is the analogon of the concentration, c , defined in Navarro et al. (1997).

The combination of Eqs. (13), (16), (17), (58), and (59) yields:

$$M(\xi) = 12M^\dagger \left[\ln(1+\xi) - \frac{\xi}{1+\xi} \right] \quad ; \quad (60)$$

$$\bar{\rho}(\xi) = 12\rho^\dagger \frac{1}{\xi^3} \left[\ln(1+\xi) - \frac{\xi}{1+\xi} \right] \quad ; \quad (61)$$

which represent the mass and mean density enclosed within a generic, isopycnic surface. It is worth noting that the profile parameter, $\nu_{\bar{\rho}} = \bar{\rho}(\Xi)/\rho^\dagger$, is linked to the dimensionless density, δ_c , defined in Navarro et al. (1997), via the relation $\delta_c = 800/\nu_{\bar{\rho}}$.

The profile parameters, ν_{mas} , ν_{inr} , and ν_{sel} , due to Eqs. (14b), (15b), (21b), and (59), after integration, take the explicit expressions:

$$\nu_{mas} = 12 \left[\ln(1+\Xi) - \frac{\Xi}{1+\Xi} \right] \quad ; \quad (62)$$

$$\nu_{inr} = \frac{4}{3} \left[\frac{\Xi(\Xi^2 - 3\Xi - 6)}{1+\Xi} + 6 \ln(1+\Xi) \right] \quad ; \quad (63)$$

$$\nu_{sel} = 36 \frac{\Xi(2+\Xi) - 2(1+\Xi) \ln(1+\Xi)}{(1+\Xi)^2} \quad ; \quad (64)$$

the velocity profile related to centrifugal support along a radial direction, by use of Eqs. (25a) and (60), is:

$$v_{eq}(\xi) = v_{eq}^\dagger \left[\frac{1}{\xi} \frac{\ln(1+\xi) - \xi/(1+\xi)}{\ln 2 - 1/2} \right]^{1/2} \left[\frac{\eta(\xi)}{\eta^\dagger} \right]^{1/2} \quad ; \quad (65)$$

and the profile parameter, ν_{anm} , due to Eq. (58), after integration, takes the explicit expression:

$$\nu_{anm} = 4\Xi \left[\frac{\Xi(2+\Xi)}{1+\Xi} - 2 \ln(1+\Xi) \right] \quad ; \quad (66)$$

which completes the specification of the physical parameters of interest, for the case under discussion.

For further analysis of the properties of mass distributions with NFW density profiles (which is outside the aim of the current paper) see e.g., Lokas & Mamon (2001).

3.2. The MOA density profile

The MOA density profile corresponds to the choice of exponents $(\alpha, \beta, \gamma) = (3/2, 3, 3/2)$ in Eq. (1). Accordingly, Eq. (2a) reads:

$$\rho(\xi) = \rho^\dagger f(\xi) \quad ; \quad f(\xi) = \frac{2}{\xi^{3/2}(1 + \xi^{3/2})} \quad ; \quad (67)$$

and Eq. (11), after integration, takes the explicit expression:

$$F(\xi) = \frac{4}{3} \ln \frac{(1 + \Xi^{1/2})^2}{1 - \Xi^{1/2} + \Xi} + \frac{8}{\sqrt{3}} \operatorname{arctg} \frac{2\Xi^{1/2} - 1}{\sqrt{3}} - \frac{4}{3} \ln \frac{(1 + \xi^{1/2})^2}{1 - \xi^{1/2} + \xi} - \frac{8}{\sqrt{3}} \operatorname{arctg} \frac{2\xi^{1/2} - 1}{\sqrt{3}} \quad ; \quad (68)$$

the combination of Eqs. (13), (16), (17), (67), and (68) yields:

$$M(\xi) = 4M^\dagger \ln(1 + \xi^{3/2}) \quad ; \quad (69)$$

$$\bar{\rho}(\xi) = 4\rho^\dagger \frac{1}{\xi^3} \ln(1 + \xi^{3/2}) \quad ; \quad (70)$$

which represent the mass and mean density enclosed within a generic, isopycnic surface.

The profile parameters, ν_{mas} and ν_{inr} , due to Eqs. (14b), (15b), (21b), and (68), after integration, take the explicit expressions:

$$\nu_{mas} = 4 \ln(1 + \Xi^{3/2}) \quad ; \quad (71)$$

$$\nu_{inr} = -4\Xi^{1/2} + \Xi^2 + \frac{4}{\sqrt{3}} \operatorname{arctg} \frac{2\Xi^{1/2} - 1}{\sqrt{3}} + \frac{4}{3} \ln(1 + \Xi^{1/2}) - \frac{2}{3} \ln(1 - \Xi^{1/2} + \Xi) + \frac{2\pi}{3\sqrt{3}} \quad ; \quad (72)$$

the profile parameter, ν_{sel} , could also be analytically integrated², but the result is exceedingly long and, in practice, unserviceable. For this reason, it has to be calculated numerically.

The velocity profile related to centrifugal support along a radial direction, by use of Eqs. (25a) and (69), is:

$$v_{eq}(\xi) = v_{eq}^\dagger \left[\frac{1}{\xi} \frac{\ln(1 + \xi^{3/2})}{\ln 2} \right]^{1/2} \left[\frac{\eta(\xi)}{\eta^\dagger} \right]^{1/2} \quad ; \quad (73)$$

and the profile parameter, ν_{anm} , due to Eq. (67), after integration, takes the explicit expression:

$$\nu_{anm} = 2\Xi \left[\Xi - \frac{2}{\sqrt{3}} \operatorname{arctg} \frac{2\Xi^{1/2} - 1}{\sqrt{3}} + \frac{2}{3} \ln(1 + \Xi^{1/2}) - \frac{1}{3} \ln(1 - \Xi^{1/2} + \Xi) - \frac{\pi}{3\sqrt{3}} \right] \quad ; \quad (74)$$

which completes the specification of the physical parameters of interest, for the case under discussion.

² By visiting the internet site: "HTTP://INTEGRALS.WOLFRAM.COM/INDEX.CGI".

3.3. The H density profile

The H density profile corresponds to the choice of exponents $(\alpha, \beta, \gamma) = (1, 4, 1)$ in Eq. (1). Accordingly, Eq. (2a) reads:

$$\rho(\xi) = \rho^\dagger f(\xi) \quad ; \quad f(\xi) = \frac{8}{\xi(1+\xi)^3} \quad ; \quad (75)$$

and Eq. (11), after integration, takes the explicit expression:

$$F(\xi) = \frac{8}{(1+\xi)^2} - \frac{8}{(1+\Xi)^2} \quad ; \quad (76)$$

the combination of Eqs. (13), (16), (17), (75), and (76) yields:

$$M(\xi) = 12M^\dagger \frac{\xi^2}{(1+\xi)^2} \quad ; \quad (77)$$

$$\bar{\rho}(\xi) = 12\rho^\dagger \frac{1}{\xi^3} \frac{\xi^2}{(1+\xi)^2} \quad ; \quad (78)$$

which represent the mass and mean density enclosed within a generic, isopycnic surface.

The profile parameters, ν_{mas} , ν_{inr} , and ν_{sel} , due to Eqs. (14b), (15b), (21b), and (76), after integration, take the explicit expressions:

$$\nu_{mas} = 12 \frac{\Xi^2}{(1+\Xi)^2} \quad ; \quad (79)$$

$$\nu_{inr} = 12 \left[\frac{\Xi(2+\Xi)}{1+\Xi} - 2 \ln(1+\Xi) \right] \quad ; \quad (80)$$

$$\nu_{sel} = 12 \frac{\Xi^3(4+\Xi)}{(1+\Xi)^4} \quad ; \quad (81)$$

the velocity profile related to centrifugal support along a radial direction, by use of Eqs. (25a) and (77), is:

$$v_{eq}(\xi) = v_{eq}^\dagger \frac{2\xi^{1/2}}{1+\xi} \left[\frac{\eta(\xi)}{\eta^\dagger} \right]^{1/2} \quad ; \quad (82)$$

and the profile parameter, ν_{anm} , due to Eq. (75), after integration, takes the explicit expression:

$$\nu_{anm} = 4\Xi \left[-\frac{\Xi(2+3\Xi)}{(1+\Xi)^2} + 2 \ln(1+\Xi) \right] \quad ; \quad (83)$$

which completes the specification of the physical parameters of interest, for the case under discussion.

3.4. Comparison with observations and simulations

Self-similar, universal density profiles are characterized by two independent parameters, i.e. a scaling density, ρ^\dagger , and a scaling radius, r^\dagger , according to Eq. (1). In some (e.g., NFW and MOA density profiles) but not all (e.g., H density profile) cases, the density must be null outside a truncation radius, to avoid an infinite, total mass. The truncation radius cannot exceed the tidal radius, due to the presence of neighbouring objects, and may safely be put equal to the virial radius (e.g., Cole & Lacey 1996; Navarro et al.

1997; Fukushige & Makino 2001; Klypin et al. 2001). In fact, the inner, denser regions of density perturbations collapse and virialize first, while the outer, less dense regions are still expanding or falling in.

High-resolution, dark matter halo simulations from hierarchical clustering in either CDM or Λ CDM scenarios, are known to be consistent with both NFW and MOA density profiles (e.g., Fukushige & Makino 2001; Klypin et al. 2001). Then the particularization of homeoidally striated, density profiles with a central cusp discussed in Sect. 2, to the special cases NFW and MOA, makes a useful tool for investigating some basic properties of large-scale celestial objects, such as galaxies or clusters of galaxies.

With regard to elliptical galaxies, some properties of the stellar subsystem are reproduced, to an acceptable extent, by H density profiles, in agreement with the observations (e.g., Hernquist 1990; Holley-Bockelmann et al. 2001). It is worth remembering that H density profiles closely approximate the de Vaucouleurs $r^{1/4}$ law for elliptical galaxies. In addition, recent observations (Geller et al. 1999; Rines et al. 2001) allow for the Coma cluster of galaxies both NFW and H density profiles, to represent the whole mass distribution within about $10h^{-1}\text{Mpc}$, for a virial radius equal to $1.5h^{-1}\text{Mpc}$. The results of the current paper were applied to the Coma cluster of galaxies in a previous attempt (Caimmi 2002), and for this reason our attention shall be restricted to elliptical galaxies, where the boundaries of the dark matter halo and the baryonic ellipsoid may safely be idealized as similar and similarly placed.

4. Application to elliptical galaxies

According to current cosmological scenarios (e.g., Navarro et al. 1997), density perturbations at recombination epoch ($z \approx 1400$) initially expand with the universe, turn around, collapse, and finally virialize (at least in their inner and denser regions). Just after virialization has been attained, baryonic and (dissipationless) non baryonic matter are expected to fill the same volume, and described by the same density profile. At late times the situation changes, as energy dissipation into heat within the gas subsystem makes it undergo further contraction, whereas the (non baryonic) dark matter does not appreciably change in extension.

Virialized density perturbations, such as elliptical galaxies and clusters of galaxies, may safely be idealized as two homeoidally striated, similar and similarly placed, density profiles with a central cusp. Our attention will be focused here on (giant) elliptical galaxies.

4.1. General considerations and main assumptions

A recent investigation performed on an optically complete sample of 42 (giant) elliptical galaxies, for which X-ray gas temperatures and central stellar velocity dispersions were

determined (Davis & White 1996), has shown evidence that (giant) elliptical galaxies contain substantial amounts of dark matter in general (Loewenstein & White 1999, hereafter quoted as LW99). Accordingly, more than about 20% and 39%-85% of the total mass within one and six optical radii, respectively, is in form of (non baryonic) dark matter, depending on the stellar density profile and observed value of X-ray gas temperature and central stellar velocity dispersion. The comparison between the velocity dispersion distributions for the dark matter and the stars, assuming isotropic orbits, shows that the dark matter is dynamically “hotter” than the stars, by a factor 1.4-2 (LW99).

The above investigation cannot be considered as conclusive in favour of the existence of dark matter haloes hosting (giant) elliptical galaxies. In fact, it has been pointed out that the attenuation (in particular, the scattering) by dust grains has the same effect on the stellar kinematics as a dark matter halo (Baes & Dejonghe 2001). On the other hand, current cosmological scenarios (CDM, Λ CDM) predict dark matter haloes hosting elliptical galaxies, as well as spiral galaxies, in the latter case supported by empirical evidence (e.g., flat rotation curves well outside optical radii). For this reason, we assume that (giant) elliptical galaxies are also embedded within dark matter haloes.

An analysis on the evolution of the physical properties of cosmological baryons at low redshifts ($z \lesssim 5$) has recently been performed (Valageas et al. 2002), which (i) yields robust model-independent results that agree with numerical simulations; (ii) recovers the fraction of matter within different phases and the spatial clustering computed by numerical simulations; (iii) predicts a soft X-ray background due to the “warm” intergalactic medium component, that is consistent with observations. The related baryon fraction in the present universe is found to be 7% in hot gas, 24% in the warm intergalactic medium, 38% in the cool intergalactic medium, 9% within star-like objects and, as a still unobserved component, 22% of dark baryons associated with collapsed structures, with a relative uncertainty no larger than 30% on these numbers. Then the amount of still undetected baryons is about one fifth of the total, one fourth of the observed baryons (intergalactic medium, stellar components, and hot gas), and at least twice the stellar-like component.

Given a typical (giant) elliptical galaxy, a natural question is to what extent the distribution of undetected baryons influences the “temperature” of both stellar and (non baryonic) dark matter. Towards this aim, we make the following main assumptions: (a) the stellar and the dark matter distributions are described by homeoidally striated, similar and similarly placed, H and NFW density profiles, respectively; (b) undetected baryons trace dark matter haloes; and (c) the virial theorem in tensor form holds for each subsystem. Let us discuss it briefly.

Elliptical galaxies embedded within dark matter haloes, may safely be idealized as two homeoidally striated, similar and similarly placed, density profiles with a central cusp. According to recent investigations (e.g., LW99), viable representations for the outer,

non baryonic, and the inner, baryonic subsystem, are NFW and H density profiles, respectively. The above mentioned mass distributions were found to be self-consistent, in a parameter range of interest, with regard to the non negativity of the distribution function (LW99) by use of a theorem due to Ciotti & Pellegrini (1992).

If undetected baryons in (giant) elliptical galaxies are present as hot gas, the gaseous subsystem is expected to be less concentrated than the stellar one, as in the Coma cluster of galaxies (e.g., Briel et al. 1992). In this respect, the simplest assumption is that undetected baryons trace the related, dark matter halo, i.e. are described by NFW density profiles.

The typical velocity dispersion components, deduced by use of the virial theorem in tensor form, are global quantities, related to the potential-energy tensors of the subsystem as a whole, and so, by construction, independent of the specific orbital distribution of the particles. This important property, however, is also a weakness of the virial theorem in tensor form, when it is used to discuss velocity dispersion components measured in the central region of a galaxy. In fact, it is well known that the related values can be significantly different for structurally identical subsystems (and so characterized by identical virial velocity dispersion components), due to different orbital structures (e.g., de Zeeuw & Franx 1991). When using central velocity dispersion components, an approach based on Jeans equations (even though still questionable) is to be preferred (e.g., Ciotti & Lanzoni 1997; LW99). On the other hand, a comparison between the results obtained by use of either above mentioned methods, may provide additional support to both of them and/or useful indications on the nature of the problem under investigation.

Strictly speaking, the central velocity dispersions (along the line of sight) in elliptical galaxies, which are deduced from observations, should be scaled to the corresponding typical values which make the virial theorem in tensor form hold (hereafter referred to, in general, as the virial velocity dispersions). Both observational evidence (e.g., Gerhard et al. 2001) and theoretical arguments (e.g., Nipoti et al. 2002) point towards the existence of dynamical homology in elliptical galaxies. In particular, a linear relation is found between a local parameter, averaged central velocity dispersion, and a global parameter, inferred maximum circular velocity, $\sigma_{0.1} = (2/3)(v_c)_{max}$ (Gerhard et al. 2001). Accordingly, the central velocity dispersion components are expected to be proportional to the virial velocity dispersion components. Then it is assumed that the related proportionality factor is of the order of unity.

In fact, typical peculiar velocity component distributions within (giant) elliptical galaxies show a maximum which is rapidly attained in the central region (at about 1 kpc), and a slow decrease occurs moving outwards (no more than about 13% the maximum at about 10 kpc), at least in the case of isotropic orbits; see e.g., LW99. Accordingly, both the central and the virial velocity dispersion components are expected to be of comparable order, slightly less than the maximum of the peculiar velocity component distri-

bution. On the other hand, most elliptical galaxies are moderately radially anisotropic (e.g., Gerhard et al. 2001), and the related variation in central velocity dispersion (an increase for increasing σ_r^2 and vice versa) is also expected to be moderate.

4.2. Input parameters, specific assumptions, and results

According to the above assumptions, a (giant) elliptical galaxy is idealized as two homeoidally striated, similar and similarly placed matter distributions, where the star and non baryonic subsystem are described by H and NFW density profiles, respectively. From this point on, the inner and the outer subsystem shall be labelled as $*$, D , instead of i , j , respectively. Let us suppose, at the moment, that undetected baryons are absent.

Following LW99, we assign to the stellar subsystem a scaling radius $r_*^\dagger = (9/20)r_{eff}$, and a truncation radius $R_* = 6 r_{eff}$, where r_{eff} is the optical effective radius. Then the truncation, scaled radius, by use of Eq. (7), is:

$$\Xi_* = \frac{R_*}{r_*^\dagger} = \frac{40}{3} ; \quad (84)$$

independent of the optical, effective radius. When the calculation of the scaling and the truncation radius is needed, the typical values:

$$r_{eff} = 5.04 h^{-1} \text{kpc} ; \quad (85)$$

$$r_*^\dagger = 2.268 h^{-1} \text{kpc} ; \quad (86)$$

$$R_* = 30.24 h^{-1} \text{kpc} ; \quad (87)$$

are used, where h is the dimensionless value of the present-day Hubble parameter, normalized to $H_0 = 100 \text{ km s}^{-1} \text{ Mpc}^{-1}$.

Turning our attention to the dark matter halo, and following again LW99, we assume for the truncation radius and the truncation, scaled radius, the typical values:

$$R_D = 256 h^{-1} \text{kpc} ; \quad (88)$$

$$\Xi_D = 10 ; \quad (89)$$

which, using Eq. (7), yield the following, typical value for the scaling radius:

$$r_D^\dagger = 25.6 h^{-1} \text{kpc} ; \quad (90)$$

in addition, the dark halo appears to be less concentrated than the stellar ellipsoid, i.e. $\Xi_D < \Xi_*$ as expected from energy dissipation due to e.g., inelastic collisions between pre-stellar clumps.

The mass ratio of non baryonic to baryonic matter related to a (giant elliptical) galaxy, equals the ratio of non baryonic to baryonic mean density within the volume of the system, $\bar{\rho}_D(R_D)/\bar{\rho}_*(R_D)$, or the ratio of non baryonic to baryonic density parameter, Ω_D/Ω_b , as (e.g., Caimmi 2002):

$$m_{D,b} = \frac{M_D}{M_b} = \frac{\bar{\rho}_D(R_D)}{\bar{\rho}_b(R_D)} = \frac{\Omega_D}{\Omega_b} = \frac{\Omega_M}{\Omega_b} - 1 ; \quad (91)$$

where $\Omega_M = \Omega_D + \Omega_b$ is the (total) matter density parameter, and $\Omega_b = (0.05 \pm 0.01)(2h)^{-2}$ fits to a good extent data on primordial nucleosynthesis (e.g., White & Fabian 1995). Accordingly, we assume the following value for the baryonic matter density parameter:

$$\Omega_b = 0.0125 h^{-2} ; \quad (92)$$

for a standard Λ CDM cosmological model with $\Omega_M = 0.3$, $\Omega_\Lambda = 0.7$, the combination of Eqs. (91) and (92) yields (Caimmi 2002):

$$m_{D,b} = 24 h^2 - 1 ; \quad (93)$$

where $5 \leq m_{D,b} \leq 23$ as $0.5 \leq h \leq 1$.

The mass of each subsystem, due to Eq. (91), keeping in mind that $M_b = M_*$ in the case under discussion, is:

$$M_* = \frac{M_T}{1 + m_{D,*}} ; \quad M_D = \frac{m_{D,*} M_T}{1 + m_{D,*}} ; \quad (94)$$

where $M_T = M_* + M_D$ is the total mass, which has to be related to the virial mass, i.e. the mass within the virial radius of the corresponding density perturbation.

Taking $h = 2^{-1/2}$ as fiducial value, and leaving $\Omega_M = 0.3$, $\Omega_\Lambda = 0.7$, Eqs. (86), (87), (88), (90), (92), and (93) yield:

$$r_*^\dagger = 3.21 \text{ kpc} ; \quad R_* = 42.77 \text{ kpc} ; \quad (95a)$$

$$r_D^\dagger = 36.20 \text{ kpc} ; \quad R_D = 362.04 \text{ kpc} ; \quad (95b)$$

$$\Omega_b = 0.025 ; \quad m_{D,*} = 11 ; \quad (95c)$$

and the combination of Eqs. (55), (56), (95a), and (95b) produces:

$$y^\dagger = 11.29 ; \quad y = 8.47 ; \quad (96)$$

the additional assumption that typical dark matter haloes hosting (giant) elliptical galaxies have masses equal to $5 \cdot 10^{12} M_\odot$, using Eqs. (94) yields:

$$M_* = 4.54 \cdot 10^{11} M_\odot ; \quad M_D = 5 \cdot 10^{12} M_\odot ; \quad M_T = 5.45 \cdot 10^{12} M_\odot ; \quad (97)$$

which completes the definition of the input parameters.

The virial theorem in tensor form may be written for each subsystem separately (e.g., Brosche et al. 1983; Caimmi & Secco 1992) as:

$$[(E_{uv})_{vir}]_{pq} + 2[(E_u)_{kin}]_{pq} = 0 ; \quad u = *, D ; \quad v = D, * ; \quad (98)$$

where $[(E_u)_{kin}]_{pq}$ represents the kinetic-energy tensor of u th subsystem. Let us define a typical velocity, $v_u \equiv [(v_u)_1, (v_u)_2, (v_u)_3]$, as:

$$[(E_u)_{kin}]_{pq} = \frac{1}{2} \delta_{pq} M_u (v_u)_p (v_u)_q ; \quad u = *, D ; \quad (99)$$

then the combination of Eqs. (14a), (57), (98), and (99) yields:

$$\frac{1}{\epsilon_{p2}\epsilon_{p3}A_p} \frac{(v_u)_p^2 (a_u^\dagger)_1}{GM_u^\dagger} = (\nu_u)_{mas}(\nu_{uv})_{vir} ; \quad u = *, D ; \quad v = D, * ; \quad (100)$$

and the additional assumption of dominant random motions implies a velocity dispersion along the line of sight, $(\sigma_u)_p = (v_u)_p$ in the special case where a principal axis points towards the observer, or using Eq. (100):

$$\frac{(\sigma_u)_p}{(\epsilon_{p2}\epsilon_{p3}A_p)^{1/2}} = \left[\frac{GM_u^\dagger}{(a_u^\dagger)_1} (\nu_u)_{mas}(\nu_{uv})_{vir} \right]^{1/2} ; \quad u = *, D ; \quad v = D, * ; \quad (101)$$

which has to be compared with its counterpart deduced from the observations. It is apparent that, in the absence of rotation, isotropy of peculiar velocity distribution occurs only for spherical configurations (*E0*), where $\epsilon_{p2}\epsilon_{p3}A_p = 2/3$, while the larger extent of anisotropy is attained for the most flattened (allowed) configurations (*E7*), where $\epsilon_{21} = \epsilon_{31} = 0.3$; $A_1 \approx 0.19$; $A_2 = A_3 \approx 0.90$; $a_1 \geq a_2 \geq a_3$.

It is worth remembering that the axis ratios and the major semiaxis, which appear in Eqs. (100) and (101), are related to the intrinsic configuration. In doing the calculations, the scaling and truncation radius will be taken as representative of the major semiaxes of the corresponding, isopycnic surface. Using the results found in Subsects. 3.1 and 3.3, together with Eqs. (95), (96), (97), and (101), the velocity dispersion along the line of sight (assumed to coincide with the direction of a principal axis) takes the value:

$$\frac{(\sigma_*)_p}{(\epsilon_{p2}\epsilon_{p3}A_p)^{1/2}} = 287 \text{ km s}^{-1} ; \quad \frac{(\sigma_D)_p}{(\epsilon_{p2}\epsilon_{p3}A_p)^{1/2}} = 225 \text{ km s}^{-1} ; \quad (102)$$

with regard to the stellar subsystem, it is consistent with a typical value $\sigma_* = 250 \text{ km s}^{-1}$ (e.g., LW99; Treu et al. 2001) except in the limiting case of (intrinsic) *E7* configurations with the major axis pointing towards the observer.

The above results hold provided the baryonic subsystem is mainly in form of stars. Let us take into consideration a different scenario, where a less concentrated gaseous subsystem than the stellar one is also present, as in the Coma cluster of galaxies (e.g., Briel et al. 1992), and assume the same mass distribution as in the non baryonic matter (Caimmi 2002). Accordingly, a (giant) elliptical galaxy may safely be conceived as formed by an inner subsystem made of stars and an outer subsystem made of gas and non baryonic matter. As the amount of baryonic and non baryonic matter have to remain unchanged, the inner and the outer subsystem are less and more massive, respectively, than in absence of undetected baryons. Again, it is assumed that the related mass distributions correspond to a H and NFW density profile, respectively. Then we define the mass ratio:

$$m_{g,*} = \frac{M_g}{M_*} ; \quad (103)$$

where M_* and M_g are the mass of the stellar and gaseous subsystem, respectively. Bearing in mind that $M_* + M_g = M_b$, where M_b is the total mass in baryons, the following relations

are easily derived:

$$M_* = \frac{M_b}{1 + m_{g,*}} \quad ; \quad M_D + M_g = \left(1 + \frac{m_{g,*}}{m_{D,*}}\right) M_D \quad ; \quad (104a)$$

$$m_{D,*} + m_{g,*} = (1 + m_{g,*})m_{D,b} + m_{g,*} \quad ; \quad (104b)$$

and the repetition of the above procedure with $M_* = M_b$, M_D , $m_{D,*} = m_{D,b}$, replaced by $M_* = M_b - M_g$, $M_D + M_g$, $m_{D,*} + m_{g,*}$, respectively, allows the specification of the input parameters.

Some output parameters, such as profile factors involving both the inner and the outer matter distribution, and velocity dispersions along the line of sight, depend on the mass of each subsystem, and then on the mass ratio of gaseous to stellar subsystem, $m_{g,*}$, via Eqs. (104). The following results are found:

$$\frac{(\sigma_*)_p / (\text{km s}^{-1})}{(\epsilon_{p2}\epsilon_{p3}A_p)^{1/2}} = 246, 223, 208, 198, 190, 184 \quad ; \quad (105)$$

$$\frac{(\sigma_D)_p / (\text{km s}^{-1})}{(\epsilon_{p2}\epsilon_{p3}A_p)^{1/2}} = 217, 213, 211, 210, 208, 208 \quad ; \quad (106)$$

$$m_{g,*} = 0.5, 1.0, 1.5, 2.0, 2.5, 3.0 \quad ; \quad (107)$$

where $m_{g,*}$ has been considered as a free parameter, in the range of interest.

It is apparent that the outer subsystem (gas plus non baryonic matter) is dynamically “hotter” than the inner, provided the gas mass fraction exceeds the star mass fraction by a factor of about 3/2. The velocity dispersion along the line of sight decreases as $m_{g,*}$ increases, and a similar trend occurs, via Eqs. (101), (103), and (104), as the total mass decreases.

On the other hand, the comparison (under the assumption of isotropic orbits) between the peculiar velocity component distributions related to the stellar ellipsoid and the dark matter halo, shows that the latter is dynamically “hotter” than the former (LW99). The reasons for this discrepancy may be due to (i) the different method used, with respect to the virial theorem in tensor form, in determining the “temperature” of the stellar ellipsoid and the dark matter halo (unfortunately, the derivation of the peculiar velocity component distribution is not outlined in LW99), and (ii) the different values of the mass ratio between the outer and inner subsystem in absence ($m_{D,*} = 11$) and in presence ($m_{D,*} + m_{g,*} = 29$), according to Eqs. (104), near equally “hot” stellar ellipsoid and dark matter halo) of undetected baryons: values $m_{D,*} + m_{g,*} > 29$ would allow dynamically “hotter” dark matter haloes, apart from the nature of their constituents.

According to a recent investigation (Valageas et al. 2002), the ratio of undetected baryons associated with collapsed structures to star-like objects, in the present universe, attains a value which is close to 2. If undetected baryons and stars are present to a similar extent within (giant) elliptical galaxies, then $m_{g,*} \approx 2$ and dark haloes, according to Eqs. (105), (106), and (107), are dynamically “hotter” than stellar ellipsoids, in the case under discussion. In this view, both the observation that the temperature of the

extended hot gas exceeds the central stellar temperature, and the fact that the non baryonic matter is dynamically “hotter” than the stars (e.g., LW99), are a reflection of the presence of undetected baryons, which trace the dark halo and are about twice as massive as the stellar ellipsoid.

Though (giant) elliptical galaxies host a surprisingly large amount of interstellar dust (up to a several ten million solar masses), most of it believed to be distributed diffusely over the galaxy (e.g., Baes & Dejonge 2001), this is still a negligible fraction of the total mass of the baryonic subsystem, such that a substantial amount of interstellar baryons within (giant) ellipticals, if it really exists, still has to be detected.

5. Concluding remarks

A general theory of homeoidally striated ellipsoids (e.g., Roberts 1962; Chandrasekhar 1969; C93), where no divergence occurs in the density profile, has been adapted to cuspy density profiles. An explicit calculation of the related, physical parameters implies the specification of the density profile, which is equivalent to the knowledge of: (i) the functional dependence of a scaled density, $f = \rho/\rho^\dagger$, on a scaled radius, $\xi = r/r^\dagger$; (ii) a boundary condition, i.e. $f(1) = 1$; (iii) two independent parameters, i.e. a scaling density, ρ^\dagger , and a scaling radius, r^\dagger ; (iv) a truncated, scaled radius, Ξ . The latter requirement is due to the fact, that the systems under consideration exhibit a null density at an infinite radius where, on the other hand, the total mass may attain a divergent value. In addition, an infinity of density profiles in the physical space, $(Or\rho)$, is represented by a single density profile in the abstract space, $(O\xi f)$, for any selected choice of exponents, (α, β, γ) , appearing in Eq. (1).

Potential-energy tensors involving both one and two, homeoidally striated density profiles, where the boundaries are similar and similarly placed, have been expressed in terms of integrals on the mass distribution. Explicit calculations have been performed for both NFW and MOA density profiles, which satisfactorily fit the results of high-resolution simulations for dark matter haloes (e.g., Fukushige & Makino 2001; Klypin et al. 2001), and for H density profiles, which closely approximate the de Vaucouleurs $r^{1/4}$ law for elliptical galaxies (e.g., Hernquist 1990; Holley-Bockelmann et al. 2001).

The virial theorem in tensor form, related to a two-component system, has been expressed for each subsystem, and applied to giant elliptical galaxies. The predicted velocity dispersion along the line of sight, in the limiting case where a principal axis points towards the observer, has been found to be consistent with the data except for (intrinsic) *E7* configurations, when the major axis points towards the observer.

The suggestion that dark matter haloes host an amount of undetected baryons as massive as about twice the stellar subsystem (Valageas et al. 2002), together with the assumption that undetected baryons trace non baryonic matter therein, has produced two

main consequences, namely (i) predicted velocity dispersions along the line of sight are lower than in absence of undetected baryons, and (ii) dark matter haloes are dynamically “hotter” than stellar ellipsoids, the transition occurring when the amount of undetected baryons is about one and a half times the stellar subsystem.

In this view, both the observation that the temperature of the extended hot gas exceeds the central stellar temperature, and the fact that the non baryonic matter is dynamically “hotter” than the stars (e.g., LW99), are a reflection of the presence of undetected baryons, which trace the dark halo and are about twice as massive as the stellar ellipsoid.

Acknowledgements. We are indebted to an anonymous referee for critical comments which made substantial improvements to an earlier version of the manuscript. The analytical integrations needed in the current paper were helped substantially by visiting the internet site: “HTTP://INTEGRALS.WOLFRAM.COM/INDEX.CGI”. This is why we are deeply grateful to the Wolfram staff, in particular to Eric Weisstein, and wish to acknowledge all the facilities encountered therein.

References

- Baes, M., Dejonge, H., 2001. ApJ 563, L19.
- Briel, U.G., Henry, J.P., Böhringer, H., 1992. A&A 259, L31.
- Brosche, P., Caimmi, R., Secco, L., 1983. A&A 125, 338.
- Bullock, J.S., Kolatt, T.S., Sigad, J., et al., 2001. MNRAS 321, 559.
- Caimmi, R., 1992. Astron. Nachr. 313, 165.
- Caimmi, R., 1993. ApJ 419, 615 (C93).
- Caimmi, R., 1995. ApJ 441, 533.
- Caimmi, R., 2002. Astron. Nachr., in press.
- Caimmi, R., Secco, L., 1992. ApJ 395, 119.
- Caimmi, R., Secco, L., 1993. Astron. Nachr. 314, 399.
- Caimmi, R., Secco, L., 2002. Astron. Nachr. 323, 13.
- Chandrasekhar, S., 1969. Ellipsoidal Figures of Equilibrium, Yale University Press, New Haven.
- Ciotti, L., Pellegrini, S., 1992. MNRAS 255, 561.
- Ciotti, L., Lanzoni, B., 1997. A&A 321, 724.
- Cole, S., Lacey, C., 1996. MNRAS 281, 716.
- Davis, D.S., White, R.E., III, 1996. ApJ 470, L35.
- de Zeeuw, T., 1985. MNRAS 216, 273.
- de Zeeuw, T., Franx, M., 1991. ARA&A 29, 239.
- Doroshkevich, A.G., 1970. Afz 6, 320.
- Fukushige, F., Makino, J., 2001. ApJ 557, 533 (FM01).
- Gerhard, O., Kronawitter, A., Saglia, R.P., Bender, R., 2001. AJ 121, 1936.
- Gheller, M.J., Diaferio, A., Kurtz, M.J., et al., 1999. ApJ 517, L23.
- Ghigna, S., Moore, B., Governato, F., et al., 2000. ApJ 544, 616.
- Hernquist, L., 1990. ApJ 356, 359.

- Holley-Bockelmann, K., Mihos, J.C., Sigurdsson, S., Hernquist, L., 2001. ApJ 549, 862.
- Jing, J.P., Suto, Y. 2002, ApJ 574, 538.
- Klypin, A., Kravtsov, A.V., Bullock, J.S., Primack, J.R., 2001. ApJ 554, 903.
- Lokas, E.L., Mamon, G.A., 2001. MNRAS 321, 155.
- Lowenstein, M., White, R.E., III, 1999. ApJ 518, 50 (LW99).
- Maller, A.H., Dekel, A., Somerville, R., 2002. MNRAS 329, 423.
- Moore, B., Governato, F., Quinn, T., Stadel, J., Lake, G., 1998. ApJ 499, L5.
- Moore, B., Quinn, T., Governato, F., Stadel, J., Lake, G., 1999. MNRAS 310, 1147.
- Navarro, J.F., Frenk, C.S., White, S.D.M., 1995. MNRAS 275, 720.
- Navarro, J.F., Frenk, C.S., White, S.D.M., 1996. ApJ 462, 563.
- Navarro, J.F., Frenk, C.S., White, S.D.M., 1997. ApJ 490, 493.
- Nipoti, C., Londrillo, P., Ciotti, L., 2002. MNRAS 332, 901.
- Rines, K., Geller, M.J., Kurtz, M.J., et al., 2001. ApJ 561, L41.
- Roberts, P.H., 1962. ApJ 136, 1108.
- Treu, T., Stiavelli, M., Bertin, G., Casertano, S., Møller, P., 2001. MNRAS 326, 237.
- White, D.A., Fabian, A.C., 1995. MNRAS 273, 72.
- White, S.D.M., 1984. ApJ 286, 38.
- Valageas, P., Schaeffer, R., Silk, J., 2002. A&A 388, 741.
- Zhao, H.S., 1996. MNRAS 278, 488.

Appendix A: A procedure for fitting simulated density profiles

Simulated, spherically averaged, virialized dark matter haloes, allow the knowledge of the density profile, the virialized mass, and the virialized radius, where the last two may safely be taken as representative of the whole mass and the whole radius, respectively (e.g., Cole & Lacey 1996; Navarro et al. 1997; Fukushige & Makino 2001; Klypin et al. 2001). A plot of the density profile on the logarithmic plane, $(O \log \xi \log f)$, necessarily implies use of dimensionless coordinates, defined by Eqs. (2a) and (6), namely:

$$f(\xi) = \frac{\rho}{\rho^\dagger} \quad ; \quad \xi = \frac{r}{r^\dagger} \quad ; \quad (A.1)$$

where the choice of the scaling density, ρ^\dagger , and the scaling radius, r^\dagger , is, in principle, arbitrary. A different choice of the above mentioned parameters, say from $(\rho^\dagger, r^\dagger)$ to $[(\rho')^\dagger, (r')^\dagger]$, makes simulated points shift by a factor, $\log[(\rho')^\dagger/\rho^\dagger]$, along the $\log f$ axis, and by a factor, $\log[(r')^\dagger/r^\dagger]$, along the $\log \xi$ axis.

In fitting simulated density profiles, our attention shall be restricted to the family of functions (e.g., Hernquist 1990; Zhao 1996):

$$f(\xi) = \frac{A}{\xi^\gamma (1 + \xi^\alpha)^\chi} \quad ; \quad \chi = \frac{\beta - \gamma}{\alpha} \quad ; \quad (A.2)$$

which has been deduced from Eqs. (1) and (A.1), provided the boundary condition:

$$\rho(r^\dagger) = \rho^\dagger f(1) = \rho^\dagger \quad ; \quad f(1) = 1 \quad ; \quad \rho^\dagger = \rho(1) \quad ; \quad (A.3)$$

holds, according to Eq. (2a). The combination of Eqs. (A.2) and (A.3) yields:

$$f(1) = A 2^{-\chi} = 1 \quad ; \quad A = 2^{\chi} \quad ; \quad (\text{A.4})$$

and Eq. (A.2) takes the final form:

$$f(\xi) = \frac{2^{\chi}}{\xi^{\gamma}(1 + \xi^{\alpha})^{\chi}} \quad ; \quad (\text{A.5})$$

which is equivalent to:

$$\log f = \chi \log 2 - \gamma \log \xi - \chi \log(1 + \xi^{\alpha}) \quad ; \quad (\text{A.6})$$

due to Eq. (A.3), the three-parameter curve represented by Eq. (A.6) remains unchanged in the logarithmic plane ($\text{O} \log \xi \log f$), for different choices of the scaling parameters, $(\rho^{\dagger}, r^{\dagger})$. On the other hand, due to Eq. (A.1), any point (ξ, f) on the curve represents different points $(\xi r^{\dagger}, f \rho^{\dagger})$ on (one or more) physical density profiles, for different choices of the scaling parameters, $(\rho^{\dagger}, r^{\dagger})$.

In the limit of negligible values of the independent variable, ξ , with respect to unity, Eq. (A.6) reduces to:

$$\log f = \chi \log 2 - \gamma \log \xi \quad ; \quad \xi \ll 1 \quad ; \quad (\text{A.7})$$

which represents, in the logarithmic plane, a straight line with slope equal to $-\gamma$ and intercept equal to $\chi \log 2$.

In the limit of preponderant values of the independent variable, ξ , with respect to unity, Eq. (A.6) reduces to:

$$\log f = \chi \log 2 - \beta \log \xi \quad ; \quad \xi \gg 1 \quad ; \quad (\text{A.8})$$

which represents, in the logarithmic plane, a straight line with slope equal to $-\beta = -(\gamma + \chi\alpha)$ and intercept equal to $\chi \log 2$.

The straight lines under discussion have coinciding intercepts i.e. they meet on the vertical axis and, in addition, represent the asymptotes of the curve, expressed by Eq. (A.6). The special cases related to NFW and MOA density profiles, are plotted in Fig. A.1.

The above results hold for $\alpha > 0$. The case $\alpha < 0$ makes the asymptotes change one into the other. The limiting case $\alpha = 0$ makes the asymptotes coincide i.e. the curve reduces to a straight line.

A change of variables:

$$x = \log \xi \quad ; \quad y = \log f \quad ; \quad (\text{A.9})$$

translates Eq. (A.6) into the equivalent form:

$$y = \chi \log 2 - \gamma x - \chi \log[1 + \exp_{10}(\alpha x)] \quad ; \quad (\text{A.10})$$

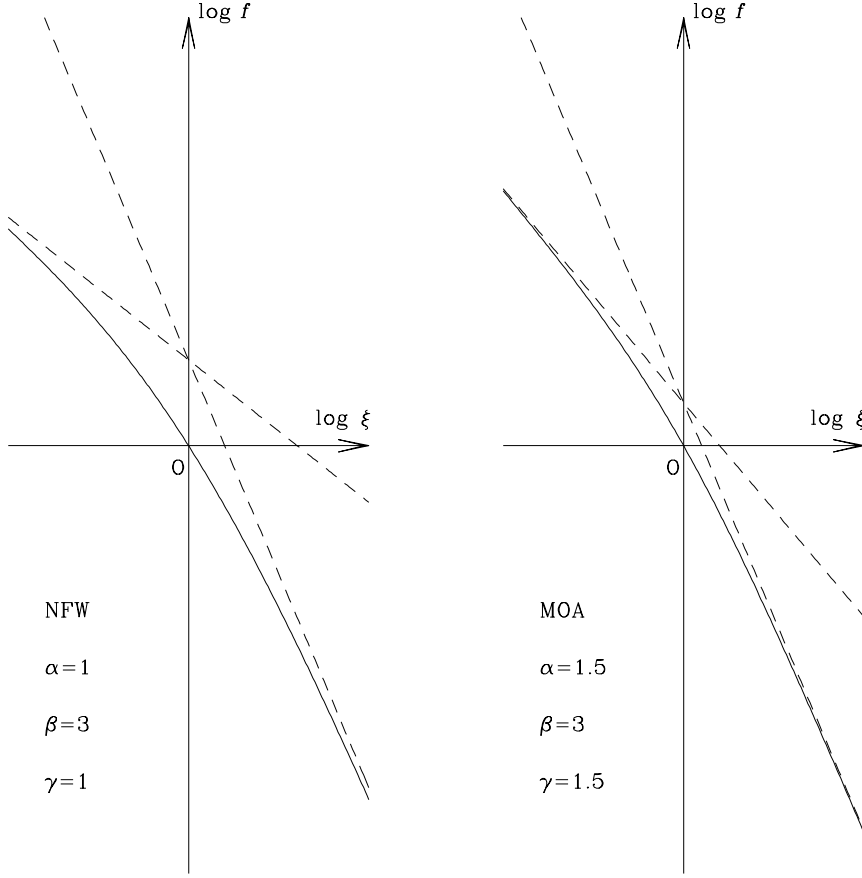


Fig. A.1. Representation, in the logarithmic plane, of NFW (left) and MOA (right) density profiles (full curves), with their asymptotes (dashed lines). In both cases, $-1 < \log \xi < +1$ and $-3 < \log f < +3$.

where, in general, $\exp_u(x) = u^x$, and $\exp(x) = e^x$, according to the standard notation. The derivatives up to the third order are:

$$\frac{dy}{dx} = -\beta + \frac{\chi\alpha}{1 + \exp_{10}(\alpha x)} ; \quad (\text{A.11a})$$

$$\frac{d^2y}{dx^2} = -\chi\alpha^2 \ln(10) \frac{\exp_{10}(\alpha x)}{[1 + \exp_{10}(\alpha x)]^2} ; \quad (\text{A.11b})$$

$$\frac{d^3y}{dx^3} = -\chi\alpha^3 \ln^2(10) \exp_{10}(\alpha x) \frac{1 - \exp_{10}(\alpha x)}{[1 + \exp_{10}(\alpha x)]^3} ; \quad (\text{A.11c})$$

and the particularization of Eq. (A.11a) to $x = 0$ i.e. $\xi = 1$ or $r = r^\dagger$, reads:

$$\left(\frac{dy}{dx} \right)_{x=0} = -\frac{1}{2}(\gamma + \beta) ; \quad (\text{A.12})$$

in the special case of NFW density profile, the right-hand side member reduces to -2, as pointed out by Bullock et al. (2001). On the other side, Eq. (A.11c) shows that the third derivative equals zero at the same point, $x = 0$ i.e. $\xi = 1$ or $r = r^\dagger$. Accordingly, density

profiles expressed by Eqs. (A.1) and (A.2), are characterized by a maximum variation in slope, in the logarithmic plane ($O \log \xi \log f$), at that point where $x = 0$ i.e. $\xi = 1$ or $r = r^\dagger$, and the slope is expressed by Eq. (A.12).

Bearing in mind that fixed points on a physical density profile change their position on the scaled density profile, for different choices of the scaling parameters, $(\rho^\dagger, r^\dagger)$, according to Eq. (A.1), a possible procedure in fitting density profiles of simulated, virialized, dark matter haloes, could be the following.

- (i) Assume that self-similar, universal density profiles, expressed by Eq. (A.5), are representative of virialized, dark matter haloes (e.g., Cole & Lacey 1996; Navarro et al. 1997; Fukushige & Makino 2001; Klypin et al. 2001).
- (ii) Select two special choices of scaling parameters, $[(\rho^\dagger)^-, (r^\dagger)^-]$ and $[(\rho^\dagger)^+, (r^\dagger)^+]$, which make simulated points well shifted on the left and on the right, respectively, i.e. (expected to be) sufficiently close to either asymptote.
- (iii) Select the best pair of deduced asymptotes, which meet together on the vertical axis.
- (iv) Calculate the slope and the intercept of either asymptote.
- (v) Calculate the exponents, (α, β, γ) , via Eqs. (A.2), (A.7) and (A.8).

In substance, the above procedure relies on the possibility, that a least-square fit related to a curve, represented by Eq. (A.6), may be reduced to a least-square fit related to a straight line, represented by either Eq. (A.7) or Eq. (A.8).

We hope that, in fitting self-similar, universal density profiles of simulated, virialized, dark matter haloes, with mass distribution expressed by Eq. (A.1), the procedure will be explained in detail.

Appendix B: Connection between NFW and MOA density profiles in fitting simulated haloes

A generic density profile, belonging to the family expressed by Eq. (1), is defined by three exponents, (α, β, γ) , and is characterized by two independent parameters e.g., a scaling density, ρ^\dagger , and a scaling radius, r^\dagger , or any other pair of independent parameters. In particular, the total mass within the virial radius, $M = M_{200}$, and a dimensionless parameter, δ , may be used, and their expression as a function of ρ^\dagger and r^\dagger are derived by fitting numerical simulations (Fukushige & Makino 2001, hereafter quoted as FM01).

Then the problem is how to compare simulated density profiles with different, theoretical ones of the kind under consideration. In doing this, our attention shall be restricted to (a) high-resolution simulations from FM01, and (b) NFW and MOA theoretical, density profiles, but the method is quite general.

With regard to NFW density profiles, the best fit to numerical simulations prescribed by FM01:

$$f(\xi) = \frac{10}{(\xi/2)[1 + (\xi/2)]^2} ; \quad (\text{B.1})$$

is inconsistent with the curve plotted in their Fig. 18 (hereafter quoted as Fig. FM18), probably due to some printing errors. In fact, the comparison with their Fig. 17 (hereafter quoted as Fig. FM17), which shows the counterpart of Eq. (B.1) related to MOA density profile:

$$f(\xi) = \frac{1}{\xi^{3/2}(1 + \xi^{3/2})} ; \quad (\text{B.2})$$

allows the following conclusions: (i) simulated density profiles remain unchanged, when both the above mentioned plots have same origin and same scale; and (ii) both NFW and MOA density profiles, represented therein, attain the same value as $\xi \rightarrow +\infty$.

With these constraints, Eq. (B.1) takes the form:

$$f(\xi) = \frac{k_1^3}{(k_1\xi)[1 + (k_1\xi)]^2} ; \quad (\text{B.3})$$

where k_1 is a parameter which can be calculated from the knowledge of the coordinates of an arbitrary selected point on the NFW density profile, plotted in Fig. FM18.

Following FM01, NFW and MOA density profiles are normalized as in Eqs. (B.1) and (B.2), respectively, and plotted in Figs. FM17 and FM18, respectively. On the other hand, Eq. (B.1) appears to be inconsistent with the curve plotted in Fig. FM18. To get a deeper insight into this problem, let us start with the obvious relations:

$$\frac{\rho}{(\rho')_{NFW}^\dagger} = \frac{\rho}{(\rho')_{MOA}^\dagger} \frac{(\rho')_{MOA}^\dagger}{(\rho')_{NFW}^\dagger} = \rho_{**} \frac{(\rho')_{MOA}^\dagger}{(\rho')_{NFW}^\dagger} ; \quad \rho_{**} = \frac{\rho}{(\rho')_{MOA}^\dagger} ; \quad (\text{B.4})$$

$$\frac{r}{(r')_{NFW}^\dagger} = \frac{r}{(r')_{MOA}^\dagger} \frac{(r')_{MOA}^\dagger}{(r')_{NFW}^\dagger} = r_{**} \frac{(r')_{MOA}^\dagger}{(r')_{NFW}^\dagger} ; \quad r_{**} = \frac{r}{(r')_{MOA}^\dagger} ; \quad (\text{B.5})$$

where ρ_{**} , r_{**} , are defined as in FM01, and $(\rho')^\dagger$, $(r')^\dagger$, have the same values as prescribed therein.

Bearing in mind that any point, $P(r_{**}, \rho_{**})$, maintains its coordinates passing from Fig. FM17 to Fig. FM18 and vice versa, the NFW density profile plotted in Fig. FM18, reads:

$$\rho_{**} = \frac{k_1 k_2}{(k_1 r_{**})[1 + (k_1 r_{**})]^2} ; \quad (\text{B.6a})$$

$$k_1 = \frac{(r')_{MOA}^\dagger}{(r')_{NFW}^\dagger} ; \quad k_2 = \frac{1}{k_1} \frac{(\rho')_{NFW}^\dagger}{(\rho')_{MOA}^\dagger} ; \quad (\text{B.6b})$$

further inspection of Figs. FM17 and FM18 discloses the validity of the condition:

$$\lim_{r_{**} \rightarrow +\infty} \frac{r_{**}^{-3/2}(1 + r_{**}^{3/2})^{-1}}{k_2 r_{**}^{-1}(1 + k_1 r_{**})^{-2}} = 1 ; \quad (\text{B.7})$$

which, performing the related calculations, is equivalent to:

$$k_2 = k_1^2 ; \quad (\text{B.8})$$

and the combination of Eqs. (B.6a) and (B.8) yields Eq. (B.3). The comparison of Eqs. (B.1), (B.2), with (58), (67), respectively, yields:

$$2(\rho^\dagger)_{MOA} = (\rho')^\dagger_{MOA} ; \quad (r^\dagger)_{MOA} = (r')^\dagger_{MOA} ; \quad (\text{B.9a})$$

$$4(\rho^\dagger)_{NFW} = k_1^3 (\rho')^\dagger_{MOA} ; \quad (r^\dagger)_{NFW} = k_1^{-1} (r')^\dagger_{MOA} ; \quad (\text{B.9b})$$

which translate the prescriptions from FM01, their Eqs. (13) and (14), into the following:

$$\rho^\dagger = C_\rho \delta \left(\frac{M}{M_{10}} \right)^{-1} \frac{10^{10} M_\odot}{\text{kpc}^3} ; \quad (\text{B.10a})$$

$$(C_\rho)_{NFW} = \frac{7k_1^3}{40} ; \quad (C_\rho)_{MOA} = \frac{7}{20} ; \quad (\text{B.10b})$$

with regard to the scaling density, ρ^\dagger , and:

$$r^\dagger = C_r \delta^{-1/3} \left(\frac{M}{M_{10}} \right)^{2/3} \text{kpc} ; \quad (\text{B.11a})$$

$$(C_r)_{NFW} = 2 \cdot 10^{-2/3} k_1^{-1} ; \quad (C_r)_{MOA} = 2 \cdot 10^{-2/3} ; \quad (\text{B.11b})$$

with regard to the scaling radius, r^\dagger , where $M_{10} = 10^{10} M_\odot$ and the values of $(\rho^\dagger)_{NFW}$, $(\rho^\dagger)_{MOA}$, are one fourth, one half, respectively, the value derived in FM01, due to the different normalization of the NFW, MOA, density profiles, adopted in the current paper. The value of the dimensionless parameter, δ , is considered to reflect an amplitude of the density fluctuation at turnaround and, for this reason, it can be thought of as constant during the evolution of a halo (e.g., Cole & Lacey 1996; Navarro et al. 1997; FM01). From the standpoint of top-hat, spherical density perturbation, it is related to both the mass and the peak height.

At this stage, what still remains to be done is the specification of the NFW density profile related to the fit of simulated, dark matter haloes from FM01 plotted in Fig. FM18. Towards this aim, let $\hat{P}(\hat{r}_{**}, \hat{\rho}_{**})$ be a selected point on the curve plotted in Fig. FM18. Accordingly, Eq. (B.3) reads:

$$\hat{\rho}_{**} = \frac{k_1^2}{\hat{r}_{**} [1 + (k_1 \hat{r}_{**})]^2} ; \quad (\text{B.12})$$

and the related, second-degree equation in k_1 has the solutions:

$$k_1^\mp = \hat{r}_{**}^{-1} \{ [1 \pm (\hat{\rho}_{**} \hat{r}_{**}^3)^{1/2}]^{-1} - 1 \} ; \quad (\text{B.13})$$

where the negative solution has no physical meaning. Then the acceptable solution to Eq. (B.12) is:

$$k_1 = \hat{r}_{**}^{-1} \{ [1 - (\hat{\rho}_{**} \hat{r}_{**}^3)^{1/2}]^{-1} - 1 \} ; \quad (\text{B.14})$$

where it is intended that the square root is non negative.

The results related to a pair of selected points on the curve plotted in Fig. FM18, are listed in Table B.1. The counterpart of Eq. (B.3) in FM01, probably due to some printing errors, is inconsistent with the results listed in Table B.1, as it would imply $k_1^3 = 10$, $k_1 = 0.5$, according to Eq. (B.1). Consistent, even if non acceptable, choices would be either $k_1^3 = 8$, $k_1 = 2$, or $k_1^3 = 10$, $k_1 = 10^{1/3} = 2.1544$.

$\hat{\rho}_{**}$	\hat{r}_{**}	k_1	k_1^2	k_1^3
1000	0.005	2.26	5.11	11.56
500	0.01	2.29	5.23	11.91

Table B.1. Specification via the parameter, k_1 , of the NFW density profile related to the fit of simulated, dark matter haloes from FM01, plotted in Fig.FM18. The coordinates of the two points, $\hat{P}(\hat{r}_{**}, \hat{\rho}_{**})$, have been deduced from Fig.FM18.